



# Carbon nitride coupled Ti-SBA15 catalyst for visible-light-driven photocatalytic reduction of Cr (VI) and the synergistic oxidation of phenol

Fenghui Liu<sup>a</sup>, Jie Yu<sup>b</sup>, Guangyuan Tu<sup>b</sup>, Ling Qu<sup>b</sup>, Jiacheng Xiao<sup>b</sup>, Yongdi Liu<sup>b</sup>, Lingzhi Wang<sup>a</sup>, Juying Lei<sup>b,\*</sup>, Jinlong Zhang<sup>a,\*</sup>

<sup>a</sup> Key Lab for Advanced Materials and Institute of Fine Chemicals, East China University of Science and Technology, 130 Meilong Road, Shanghai 200237, PR China

<sup>b</sup> State Environmental Protection Key Laboratory of Environmental Risk Assessment and Control on Chemical Process, East China University of Science and Technology, 130 Meilong Road, Shanghai 200237, PR China

## ARTICLE INFO

### Article history:

Received 4 May 2016

Received in revised form 26 July 2016

Accepted 1 August 2016

Available online 1 August 2016

### Keywords:

Ti-SBA15-CN  
Photocatalysis  
Visible light  
Cr (VI)  
Phenol

## ABSTRACT

In this study, carbon nitride was loaded into the titanium incorporated SBA-15 mesoporous silica (denoted as Ti-SBA15-CN) by a two-step vapor condensation of dicyandiamide. The as-prepared sample was characterized by various spectroscopy techniques. Photocatalytic reduction of Cr (VI) in aqueous solution was investigated using Ti-SBA15-CN under visible-light irradiation. By introducing Ti into the SBA-15 framework structure, the visible light driven photocatalytic activity of the obtained Ti-SBA15-CN was higher than SBA15-CN and the photocatalytic activity exhibited a rise with the increase of Ti contents. It was because the presence of Ti moiety could promote the separation of the photo-generated charge carriers in carbon nitride, leading to the enhancement of the photocatalytic activity. The addition of phenol further enhanced the photocatalytic reduction of Cr (VI). Similarly, the presence of Cr (VI) promoted the degradation of phenol. The synergistic effect between the reduction of Cr (VI) and the degradation of phenol provided salutary method for purification of the complex waste water and environmental restoration.

© 2016 Elsevier B.V. All rights reserved.

## 1. Introduction

Cr (VI) had been listed as one of the priority pollutants by the United States Environmental Protection Agency (USEPA) [1,2], due to its proverbially toxicity, mutagenic and carcinogenic activity to human beings when its concentration level was higher than 0.05 ppm in drinking water. Hence, the reduction or disposal of Cr (VI) ions had received great attention in the wastewater purification processes. Currently, the common methods for the removal of Cr (VI) were precipitation, cementation, coagulation, ion exchange, reverse osmosis, electro-dialysis, electro-coagulation [3] and photocatalytic reduction [4,5]. In consideration of solar energy conversion, photocatalytic reduction was an active, valid, and clean technology for Cr (VI) reduction in aqueous media. The Cr (VI) could be photoreduced to the less harmful Cr (III) during the photocatalytic process. On the other hand, organic pollutants like phenol in

water also have been causing serious environmental problems. It was well-known that the phenol was noxious, erosive and could cause respiratory, nervous and cardiovascular problems [6]. Therefore, it has been essential to find an effective way to control the levels of organic pollutants in water.

The co-existence of organic pollutants and heavy metal ions in wastewater is a common phenomenon, and the simultaneous removal of organic pollutants and metal ions from wastewater has particular significance to pollution control and remediation. Prairie et al. [7] had observed that the metal ions Cr (VI), Au (III), Pt (IV), Hg (II), Ag (I), and Cu (II) could be quickly removed in the presence of salicylic acid with TiO<sub>2</sub> photocatalyst under UV illumination, which was the first to describe a synergistic relationship in the photocatalytic process between reduction of metal ions and oxidation of organic matter. The basis of this synergistic effect was that photo-generated electron-hole pairs were consumed separately in the corresponding redox and oxidation half-reactions, which could significantly prevent the recombination of electron-hole pairs and enhance the photocatalytic efficiency [8].

Recently, more efforts had been devoted to exploring efficient photocatalyst for Cr (VI) reduction, for example, TiO<sub>2</sub> could effec-

\* Corresponding authors.

E-mail addresses: [leijuying@ecust.edu.cn](mailto:leijuying@ecust.edu.cn) (J. Lei), [jlzhang@ecust.edu.cn](mailto:jlzhang@ecust.edu.cn) (J. Zhang).

tively reduce Cr (VI) to Cr (III) [9]. In addition, the reduction rate of Cr (VI) could increase in the presence of organic pollutants such as phenol. Subrahmanyam [10] reported the simultaneous treatment of phenol and Cr (VI) was advantageous over individual treatments by using the C-doped TiO<sub>2</sub> nanomaterials in simulated solar light. Huang et al. [11] synthesized porous single crystalline ZnO nanoplates for Cr (VI) reduction and phenol degradation under UV irradiation. However, there have been few reports on the high-performance catalysts for the simultaneous removal of Cr (VI) and phenol under visible light.

Graphitic carbon nitride has been considered to be a fascinating candidate for photocatalysis owing to the visible-light driven band gap, high thermal and chemical stability [5,12–14]. However, bulk carbon nitride had low surface area and was also limited by the high recombination rate of photo-generated electrons and holes [15–17].

In this study, carbon nitride was loaded into the channel of mesoporous silica SBA-15 and a catalyst with larger specific surface area was synthesized. Meanwhile, the composition of the pore wall of the SBA-15 was adjusted by introducing Ti into the framework. Through the interaction between the Ti and the carbon nitride, the separation of photo-generated electrons and holes was promoted, thus the photocatalytic activity for Cr (VI) reduction was improved for Ti-SBA15-CN. The synergistic effect between Cr (VI) reduction and phenol oxidative degradation was also investigated and the synergistic photocatalytic mechanisms were proposed.

## 2. Experimental

### 2.1. Chemicals

Pluronic P123 was purchased from Aldrich reagent plant. Dicyandiamide was obtained from Aladdin Industrial Corporation. Hydrochloric acid, tetraethoxysilane, tetra butyl titanate, potassium dichromate (K<sub>2</sub>Cr<sub>2</sub>O<sub>7</sub>), phenol were all got from Shanghai Lingfeng Chemical Reagent Factory. All reagents were used as received without further purification. Deionized water was used throughout all experiments.

### 2.2. Synthesis of the Ti activated mesoporous silica (SBA-15) composites

The SBA-15 composites were prepared using Pluronic P123 as the template by a method similar to that described before [18]. Typically, Pluronic P123 (EO<sub>20</sub>PO<sub>70</sub>EO<sub>20</sub>, M<sub>av</sub> = 5800, Aldrich) (0.5 g) was dissolved in 2.0 M HCl solution (120 mL) to get a homogeneous solution by vigorous stirring at 38 °C. Then, TEOS (9 mL) and appropriate volume of TBOT were added and the mixture was stirred continually for 24 h at 38 °C. The volume ratio of TEOS and TBOT was controlled at 50:1, 100:1, and 150:1. Subsequently, the mixture was transferred into an autoclave and hydrothermal at 100 °C for 24 h. Then the samples were filtered, washed with deionized water for three times, dried at 60 °C under vacuum condition, and then calcinated at 550 °C for 6 h. The heating rate was 1 °C min<sup>-1</sup>. The obtained samples with TEOS/TBOT ratios of 50:1, 100:1, 150:1 were named as 50:1 Ti-SBA15, 100:1 Ti-SBA15, and 150:1 Ti-SBA15 respectively.

### 2.3. Synthesis of the Ti-SBA15-CN

The carbon nitride was loaded into Ti-SBA15 in a program-controlled furnace. 2 g of dicyandiamide (DCDA) was placed in a porcelain ark, and then spread 0.35 g of Ti-SBA15 on it. The porcelain ark was wrapped with aluminum foil paper poked a few holes. The temperature was firstly increased to 250 °C in 30 min and kept for 2 h and then increased to 550 °C for further 4 h. The resultant

Ti-SBA15 samples were denoted as SBA15-CN, 50:1Ti-SBA15-CN, 100:1Ti-SBA15-CN, and 150:1Ti-SBA15-CN, respectively. Herein, this work provided a new and simple method to prepare Ti-SBA15-CN which could efficiently use raw materials. Besides that, this was also a high efficient method because of no solvent consumption.

### 2.4. Characterization

The morphology of as-prepared Ti-SBA15-CN series samples were characterized by transmission electron microscopy (TEM, JEM2000EX). XRD patterns which were conducted to identify the samples' microstructure characteristics, were recorded on a Rigaku D/MAX-2550 diffract meter using Cu K $\alpha$  radiation of wavelength 1.5406 Å, typically running at a voltage of 40 kV and current of 100 mA. UV-vis absorbance spectra were achieved for the dry-pressed disk samples using a Scan UV-vis spectrophotometer (SHIMADZU, uv-2450), and using BaSO<sub>4</sub> as a reflectance sample. BET surface area measurements were carried out by N<sub>2</sub> adsorption at 77 K using an ASAP2020 instrument. By utilizing the Barrett-Joyner-Halenda (BJH) model, the pore volumes and pore size distributions were got from the adsorption branches of isotherms. X-ray photoelectron spectroscopy (XPS) studies were taken by a Perkin-Elmer PHI 5000CESCA system with Al K $\alpha$  radiation operated at 250 W. FTIR of the samples were recorded in transmission mode from KBr pellets at room temperature on a Bruker Tensor spectrometer with a resolution of 4 cm<sup>-1</sup>, using 32 scans per spectrum in the region of 400–4000 cm<sup>-1</sup>. The mass ratio of every sample to KBr was constant at 1:200. TG measurements of the catalysts were conducted on a Netzsch TG 209 F3 apparatus. The samples were placed in  $\alpha$ -Al<sub>2</sub>O<sub>3</sub> crucibles and heated in flowing air (20 mL min<sup>-1</sup>) from room temperature to 800 °C at a rate of 20 °C min<sup>-1</sup>. The analysis of photoluminescence spectra (PL) and time resolved PL decay spectra was carried out at room temperature using a PTI QM-4 fluorescence spectrophotometer. All the electrochemical experiments included electro-chemical impedance spectroscopy and photocurrents measurements were carried out on an electrochemical analyzer (CHI 660 D electrochemical station, CHI Instruments Inc.) at room temperature. A standard three-electrode system consisting of a working electrode (as-prepared samples as the working electrodes with an active area of ca. 0.5 cm<sup>2</sup>), a Pt wire as the counter electrode and a saturated Ag/AgCl as the reference electrode was employed. Transient photocurrent responses of different samples were carried out in 0.5 M Na<sub>2</sub>SO<sub>4</sub> aqueous solution under various irradiation conditions (300 W Xe lamp). The EIS measurements were performed in the presence of a 25 mmol L<sup>-1</sup> K<sub>3</sub>Fe(CN)<sub>6</sub> and K<sub>4</sub>Fe(CN)<sub>3</sub> and 0.1 mol L<sup>-1</sup> KCl mixture aqueous solution. Phenol and its degradation byproducts were analyzed by HPLC. Separation was obtained with a C18 column. The eluting solvent was methanol and water 55/44% v/v at a flow rate of 0.5 mL min<sup>-1</sup>. The wavelengths of analyses for phenol and 1,4-benzoquinone, catechol and hydroquinone were done at 271, 244, 276 and 290 nm, respectively. The products were identified by comparison of retention times with standards.

### 2.5. Photocatalytic activity test

The photocatalytic activities of the products were tested for the removal of Cr (VI) under visible light irradiation. A 300 W xenon lamp with a 420 nm cutoff filter was chosen as the visible light source. In a typical experiment, 50 mg photocatalyst was suspended in 50 mL Cr(VI) (K<sub>2</sub>Cr<sub>2</sub>O<sub>7</sub>) aqueous solution (10 mg/L) with or without the addition of phenol. And the pH of the suspension was adjusted by using 0.1 M HCl solution and 0.1 M NaOH solution. The resulting suspensions in the quartz tube were then stirred in the dark for 0.5 h to establish adsorption–desorption equilibrium between the photocatalyst and Cr (VI) before irradiation. During

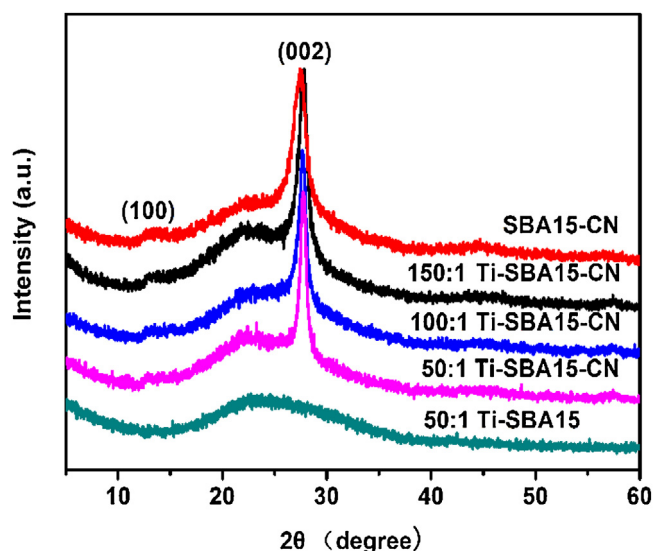


**Fig. 1.** Wide-angle XRD patterns of 50:1 Ti-SBA15, SBA15-CN and Ti-SBA15-CN with various Ti dosages.

the visible light irradiation, about 4 mL of the suspensions was taken from the reaction cell at given time intervals, and then being centrifuged to remove the photocatalyst particles. The concentration of Cr (VI) was determined by the diphenylcarbazide (DPC) method [11]. The absorbance of sample solutions was measured by an UV-vis spectrometer at 540 nm after full color development. The concentration of phenol was measured by a HPLC system.

### 3. Results and discussion

#### 3.1. Characterization results

##### 3.1.1. XRD measurement

Fig. 1 showed the wide-angle XRD patterns of 50:1 Ti-SBA15, SBA15-CN and Ti-SBA15-CN with various Ti dosages. As shown in the figure, a broad peak at  $22^\circ$  was attributed to amorphous silica [18,19]. By comparison with the diffraction peaks of 50:1 Ti-SBA15, the diffraction peak at around  $27.4^\circ$  was corresponded to the accumulation of conjugate aromatic ring plane structure in carbon nitride and the small diffraction peak at about  $13.1^\circ$  was attributed to the tri-s-triazine unit of carbon nitride [20,21]. These two peaks together proved the successful synthesis of carbon nitride. The

**Table 1**

Specific surface area, pore volume and pore size of SBA-15, Ti-SBA15 and Ti-SBA15-CN photocatalysts.

Samples	$S_{\text{BET}}/\text{m}^2 \text{ g}^{-1}$	Pore volume/ $\text{cm}^3 \text{ g}^{-1}$	Pore size/nm
SBA-15	565.54	0.87	5.63
150:1 Ti-SBA15	470.69	0.73	5.63
100:1 Ti-SBA15	373.31	0.62	5.62
50:1 Ti-SBA15	362.60	0.61	5.56
SBA15-CN	54.10	0.14	3.58
150:1 Ti-SBA15-CN	61.07	0.17	3.64
100:1 Ti-SBA15-CN	54.99	0.15	3.62
50:1 Ti-SBA15-CN	73.67	0.19	3.68

Bragg crystalline Ti containing phases (e.g.  $\text{TiO}_2$ ) were not detected at  $25.3^\circ$  and  $48^\circ$  related to anatase phase of titania [22–24], this might because the quantity of the titanium was not enough to be detected by XRD.

##### 3.1.2. The $\text{N}_2$ adsorption-desorption measurement

The  $\text{N}_2$  adsorption-desorption measurement was performed to illuminate characteristics of Ti-SBA15 and Ti-SBA15-CN. According to the IUPAC classification, the isotherms of Ti-SBA15 were of type IV in Fig. 2a, along with a steep H1 hysteresis loop in the range of  $P/P_0 = 0.5\text{--}0.8$ , indicating that the samples possessed typical mesoporous structures [25–27]. Table 1 showed the structural features of the prepared catalysts. We could see that SBA-15 had the largest BET surface area of  $565.54 \text{ m}^2 \text{ g}^{-1}$  and the largest pore volume of  $0.87 \text{ cm}^3 \text{ g}^{-1}$ , while an increase of Ti moiety in the silica framework led to a decrease in surface area and pore volume of Ti-SBA15.

After loading carbon nitride into the Ti-SBA15, the mesoporous structure of Ti-SBA15-CN was maintained (Fig. 2b). Nevertheless, the surface area and pore volume, as well as pore size of Ti-SBA15 decreased apparently, as presented in Table 1. The reason might be that the high loading amounts of DCDA could result in the complete dispersion on the interior walls of mesopores in Ti-SBA15. As a result, the supported carbon nitride on Ti-SBA15 was probably well-dispersed polymerized networks, and the corresponding pore sizes and pore volume of Ti-SBA15-CN samples decreased.

##### 3.1.3. TEM measurement

TEM was further used to verify the mesoporous structure and the morphology of Ti-SBA15 and Ti-SBA15-CN photocatalysts. Fig. 3 showed the TEM images of SBA-15, SBA15-CN, 50:1 Ti-SBA15 and 50:1 Ti-SBA15-CN. As shown in Fig. 3a and c, both SBA-15 and Ti-SBA15 presented highly ordered mesoporous structures, which were consistent with the  $\text{N}_2$  adsorption-desorption isotherms

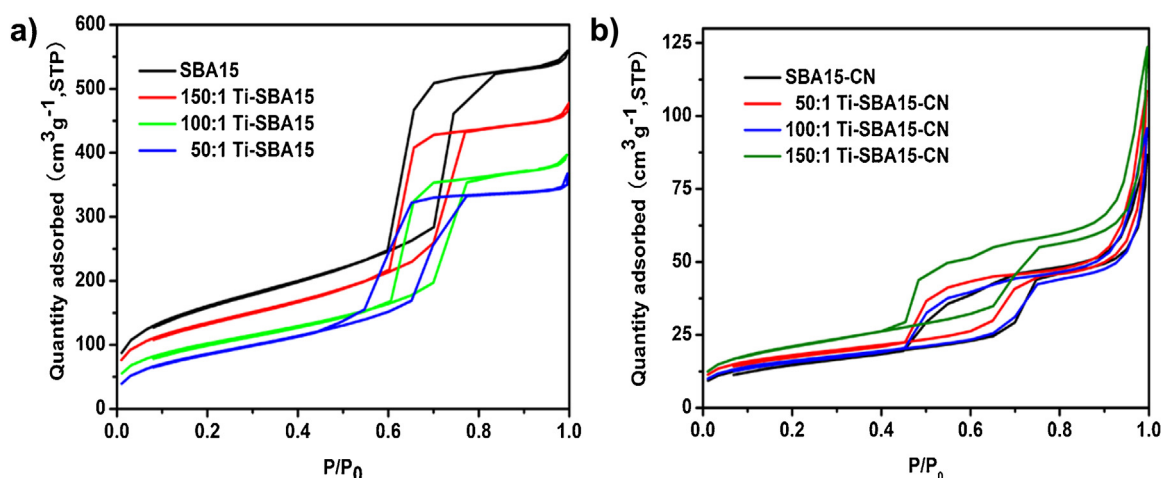


**Fig. 2.**  $\text{N}_2$  adsorption-desorption isotherms of (a) SBA-15 and Ti-SBA15 series sample, (b) Ti-SBA15-CN series sample.



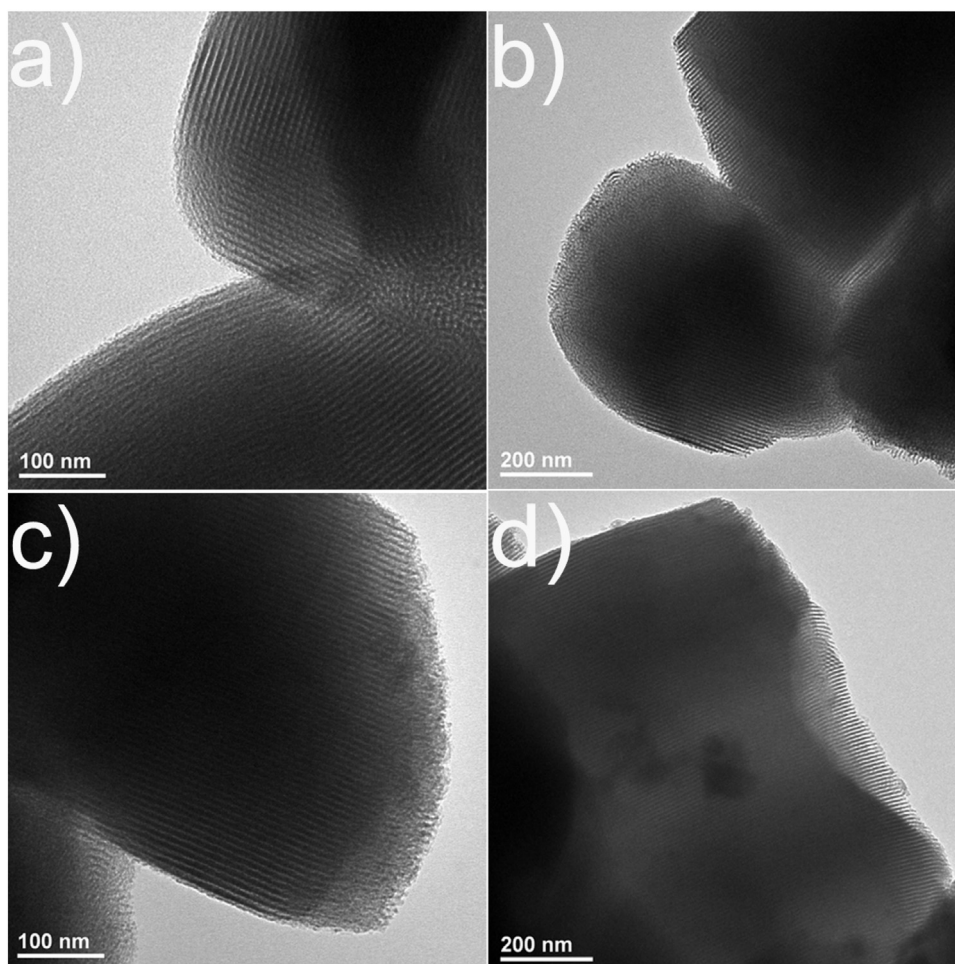


Fig. 3. TEM images of (a) SBA15, (b) SBA15-CN, (c) 50:1 Ti-SBA15, (d) 50:1 Ti-SBA15-CN.

(Fig. 2a). As for Ti-SBA15-CN in Fig. 3b and d, the mesopores of Ti-SBA15 had been partially filled with carbon nitride materials without obvious aggregation of carbon nitride observed and the hollow mesostructures were dominant, implying the well dispersion of carbon nitride in Ti-SBA15.

#### 3.1.4. FTIR measurement

Fig. 4 showed the FTIR spectra of 50:1 Ti-SBA15, 50:1 Ti-SBA15-CN and SBA15-CN. Three bands at 470, 806, and 1089  $\text{cm}^{-1}$  were revealed by the spectrum of 50:1 Ti-SBA15, which were attributed to the condensed silica (Si-O-Si (Ti)) network [28]. For Ti-SBA15-CN materials, strong bands at 1241, 1322, 1406, 1571, and 1631  $\text{cm}^{-1}$  were corresponding to the typical stretching modes of CN heterocycles [29,30] and the band at 806  $\text{cm}^{-1}$  [31] was attributed to the characteristic breathing mode of triazine units. All of these implied the successful loading of carbon nitride onto Ti-SBA15. Comparing with the FTIR of 50:1 Ti-SBA15, the FTIR band at 470  $\text{cm}^{-1}$  could be found in Ti-SBA15-CN, proving the presence of the [Si-O] framework of mesoporous structures in Ti-SBA15-CN. In addition, we could also observe the broad bands at 2000–3600  $\text{cm}^{-1}$  for all the samples, which correspond to the physically adsorbed  $\text{H}_2\text{O}$  and  $\text{CO}_2$  from the atmosphere [29].

#### 3.1.5. XPS analysis

Additionally, the surface chemical environment was analyzed by XPS. The survey spectrum of Ti-SBA15-CN (Fig. 5a) revealed that the main elements of the sample were C, N, Si, O and Ti. Among them, the Si and O were mainly derived from the SBA-15 support.

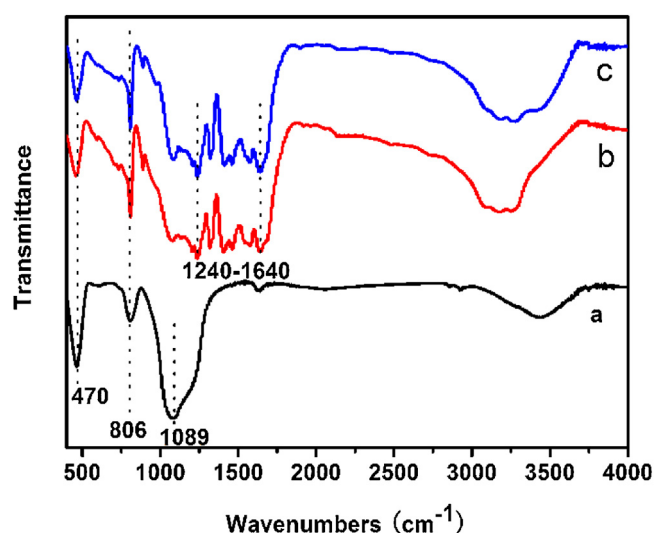


Fig. 4. FTIR spectra of (a) 50:1 Ti-SBA15, (b) 50:1 Ti-SBA15-CN, (c) SBA15-CN.

As displayed in Fig. 5b, the C1s peak at 286.0 eV can be assigned to the  $\text{sp}^2$ -type C=N bonds. And the peak at 284.7 eV was belong to the C-C bonds. For the N 1s core level in Fig. 5c, the first band at 398.7 eV was originated from nitrogen atoms which had two neighbors, while the second one at 400.3 eV was attributed to nitrogen atoms having three neighbors [32,33].

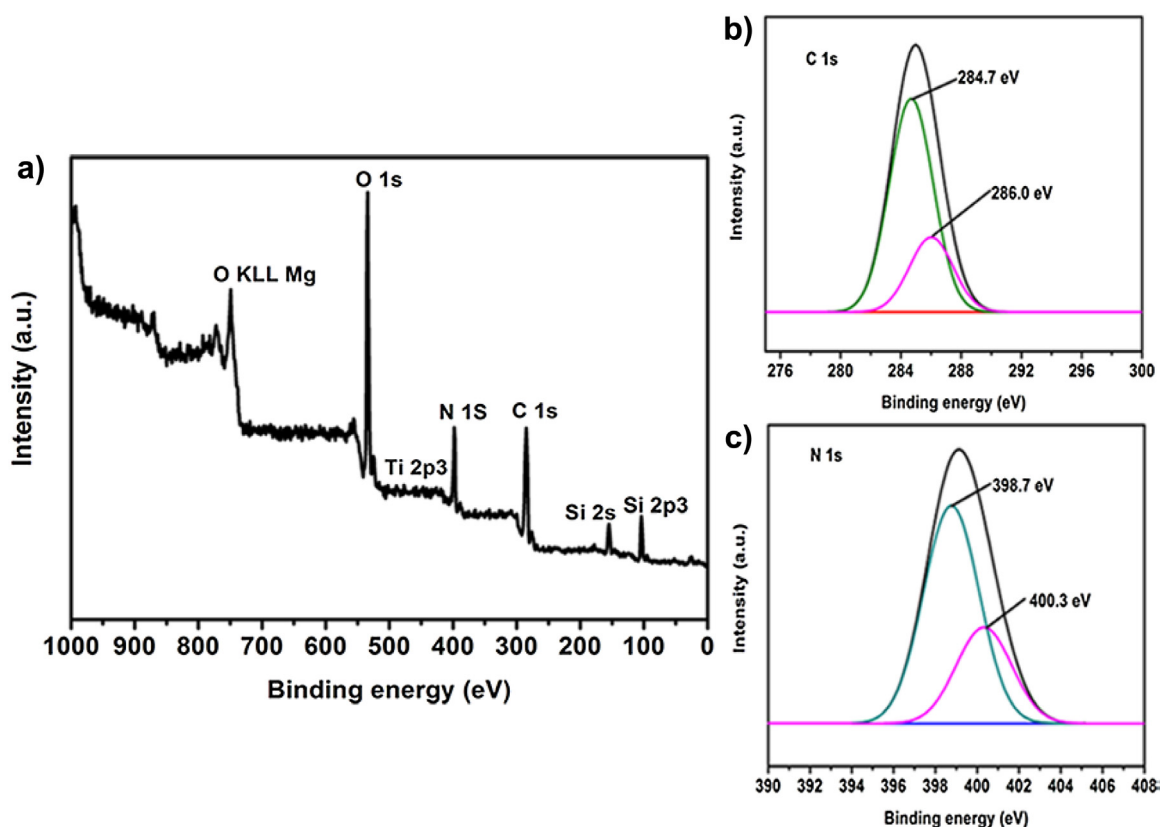


Fig. 5. XPS spectra of Ti-SBA15-CN (a) survey scan; (b) deconvoluted C 1s and (c) deconvoluted N 1s.

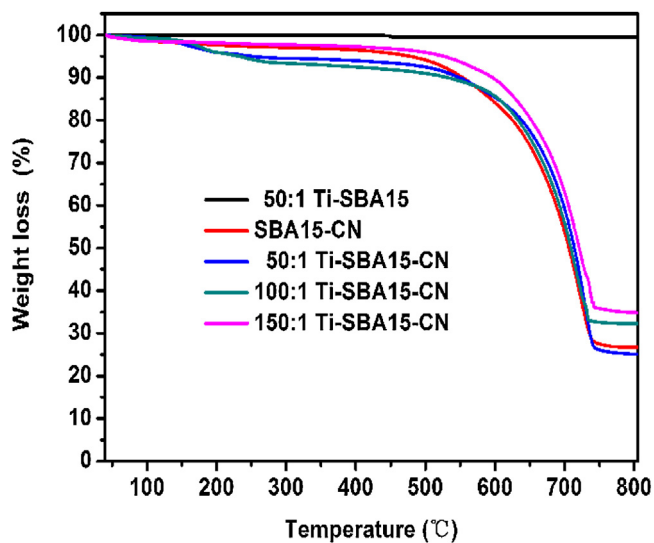


Fig. 6. TG curves of different materials.

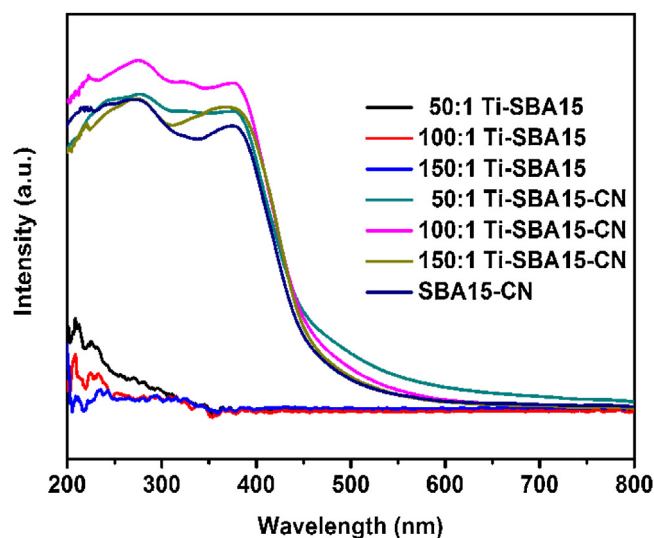


Fig. 7. UV–vis adsorption spectra of different materials.

### 3.1.6. TG analysis

TG measurement was applied to analyze the actual loading amounts of carbon nitride on Ti-SBA15. The bare 50:1 Ti-SBA15 sample revealed a negligible weight loss (0.5 wt%) from 40 to 800 °C in Fig. 6, which was attributed to its physically adsorbed water. As to Ti-SBA15-CN, apart from weak weight loss below 250 °C, we could find that the materials were thermally stable in a wide range of temperatures. As the temperatures were elevated above 550 °C, the TG curves presented clear declines as carbon nitride started to self-decompose and finished the total decomposition at 750 °C. Based on the TG curves, the loading amounts of carbon nitride were

calculated to be 73.2, 74.8, 67.8, 65.2 wt% for SBA15-CN, 50:1 Ti-SBA15-CN, 100:1 Ti-SBA15-CN, 150:1 Ti-SBA15-CN, respectively.

### 3.1.7. UV–vis measurement

UV–vis measurement was used to investigate the local structure of Ti moieties incorporated within SBA-15 frameworks. Ti-SBA15 exhibited a typical absorption peak at around 210 nm in Fig. 7. This clear absorption was obviously much shorter than the maximum absorption wavelength of TiO<sub>2</sub> nanocrystallite and could be assigned to the ligand-to-metal charge transfer (LMCT) absorption of highly dispersed Ti species [34–40]. The absorption band

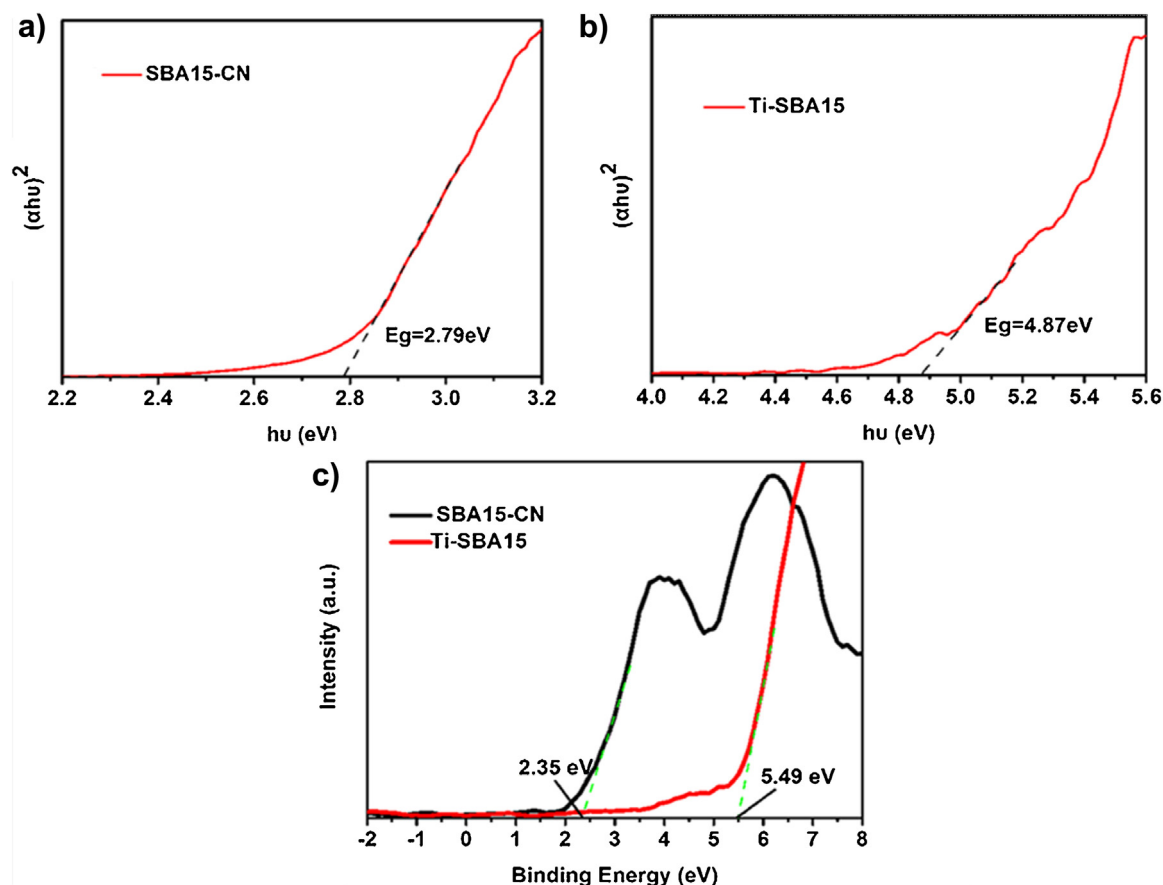


Fig. 8. (a) Tauc plot for band gap determination of SBA15-CN, (b) Tauc plot for band gap determination of 50:1Ti-SBA15, (c) VB XPS of the SBA15-CN and 50:1 Ti-SBA15.

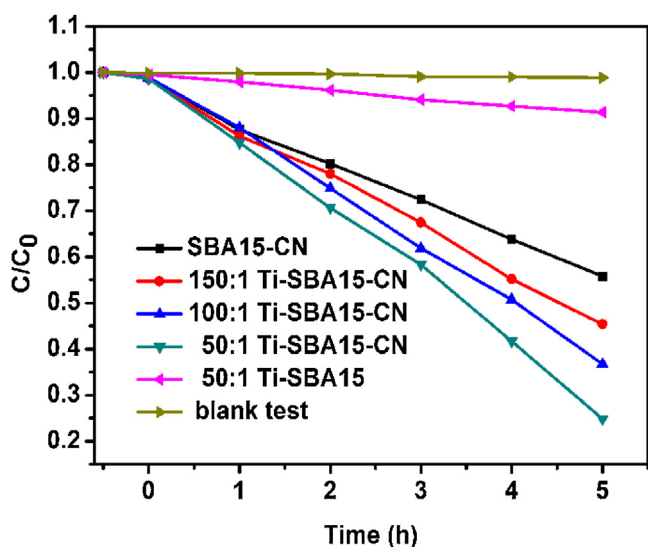


Fig. 9. Photocatalytic reduction of Cr (VI) (10 mg/L) over Ti-SBA15-CN under visible light irradiation ( $\lambda > 420 \text{ nm}$ ). (blank test: reduction of 10 mg/L Cr (VI) without catalyst).

at 200–240 nm and 240–280 nm were attributed to the isolated tetrahedral Ti-oxide monomers and dimers or small oligomers, respectively [34–40]. In the case of Ti-SBA15-CN, all the samples showed similar adsorption in visible light region and the optical absorbance of Ti-SBA15-CN photocatalysts was slightly higher than SBA15-CN. This suggested the interaction between carbon nitride and Ti moiety could possibly cause change in the process

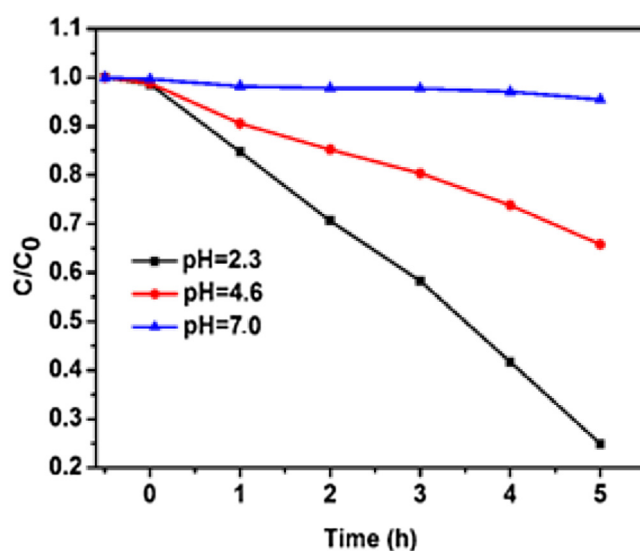


Fig. 10. Effect of pH on the reduction of Cr (VI) (10 mg/L) with 50:1 Ti-SBA15-CN under visible light irradiation ( $\lambda > 420 \text{ nm}$ ).

of electron-hole pair formation, which would be favorable for the photocatalytic reaction.

The UV–vis adsorption spectra were also used to determine the conduction band (CB) and valence band (VB) positions of SBA15-CN and Ti-SBA15 with the assistance of VB XPS spectra. From the Tauc plot (Fig. 8a and b) obtained from UV–vis adsorption spectra, the band gap of the SBA15-CN and Ti-SBA15 (represented by 50:1Ti-SBA15) could be calculated. The obtained band gap values

were 2.79 eV and 4.87 eV for SBA15-CN and 50:1Ti-SBA15, respectively. The VB position of SBA15-CN and 50:1Ti-SBA15 was further analyzed through VB XPS spectra (Fig. 8c). We could find that the position of the VB edge of SBA15-CN was located at about 2.35 eV, which was consistent with Guo's report [41], whereas the VB edge of 50:1Ti-SBA15 was located at 5.49 eV. Based on the above results, we could calculate that the CB values were  $-0.44$  eV and  $0.62$  eV for SBA15-CN and 50:1Ti-SBA15. Since the CB values of SBA15-CN was more negative than that of Ti-SBA15, the photo-generated electrons on carbon nitride could be easily transferred to the Ti moiety, causing the effective separation of the photo-generated electron-hole pairs.

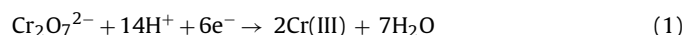
### 3.2. Photocatalytic performances

#### 3.2.1. Photocatalytic reduction of Cr (VI)

In order to understand the visible light photocatalytic activity of the as-synthesized samples, a test reaction was carried out for the reduction of 10 mg/L of Cr (VI) with 50 mg of the catalyst and the results were shown in Fig. 9.

As can be seen from Fig. 9, in the presence of 50:1 Ti-SBA15, the reduction of Cr (VI) hardly occurred under visible-light irradiation. Instead, the reduction of Cr (VI) proceeded rapidly in the presence of carbon nitride. In addition, it could be seen that all of the Ti-SBA15-CN exhibited higher photocatalytic activity than SBA15-CN, indicating interactions between carbon nitride and Ti moiety in the SBA-15 framework. In addition, with the increase of Ti contents, the photocatalytic activity of Ti-SBA15-CN exhibited a rise. It was maybe because the photo-generated electrons in conduction band of carbon nitride could be easily transferred to the Ti moiety in the Ti-SBA15-CN photocatalysts and with the increase of Ti contents, much more electrons and holes in carbon nitride were separated, achieving higher photocatalytic activity.

It's worth noting that, in the above photocatalytic experiments, the pH for the reaction system was all set at an acid value of  $\text{pH} = 2.3$ . According to previous reports [11], Cr (VI) ion ( $\text{Cr}_2\text{O}_7^{2-}$ ) was generally the predominant species at medium to low pH values, the reduction of Cr (VI) by photogenerated electrons could be described as follows:



As shown in Eq. (1), the pH could strongly effect the reduction of Cr (VI) to Cr (III) and a decrease of pH could expectedly increase the reducibility of Cr (VI). On the other hand, Cr (III) could become  $\text{Cr(OH)}_3$  which would be precipitated on the surface of the photocatalysts at increased solution pH, covering the activity sites of the catalysts. For comparison, we also did the experiments at higher pH values of 4.6 and 7.0 with other experimental conditions unchanged. As shown in Fig. 10, apparently, the Cr (VI) reduction efficiencies were much higher at  $\text{pH} = 2.3$  than those at  $\text{pH} = 4.6$  and  $\text{pH} = 7.0$ . Hence, the suitable pH of photo-reduction of Cr (VI) in our work was recommended as  $\text{pH} = 2.3$  and further experiments were all conducted at this pH.

#### 3.2.2. Effect of phenol concentration on the removal of Cr (VI)

Based on the photocatalytic theory and the synergistic effect between organic compounds and metal ions, phenol was chosen as a representative pollutant to investigate the synergistic effect between Cr (VI) reduction and phenol oxidative degradation. The effect of variable initial concentration of phenol on the reduction of 10 mg/L Cr (VI) at  $\text{pH} = 2.3$  was described in Fig. 11. With phenol concentration increasing from 0 to 30 mg/L, the reduction efficiency of Cr (VI) increased accordingly, suggesting that the existence of phenol could enhance the removal of Cr (VI) by acting as the scavenger of photo-generated holes. For example, with the addition of

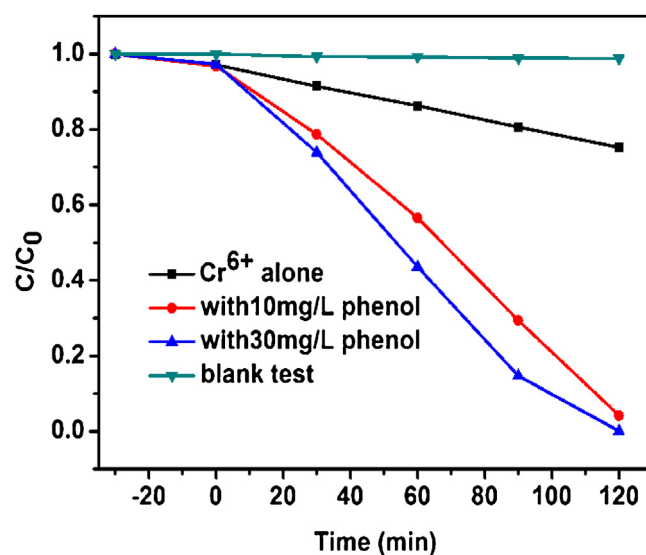


Fig. 11. Effect of phenol concentration on the photocatalytic reduction of Cr (VI) (10 mg/L) by using 50:1 Ti-SBA15-CN under visible light irradiation (blank test: reduction of 10 mg/L Cr (VI) with 10 mg/L phenol without catalyst).

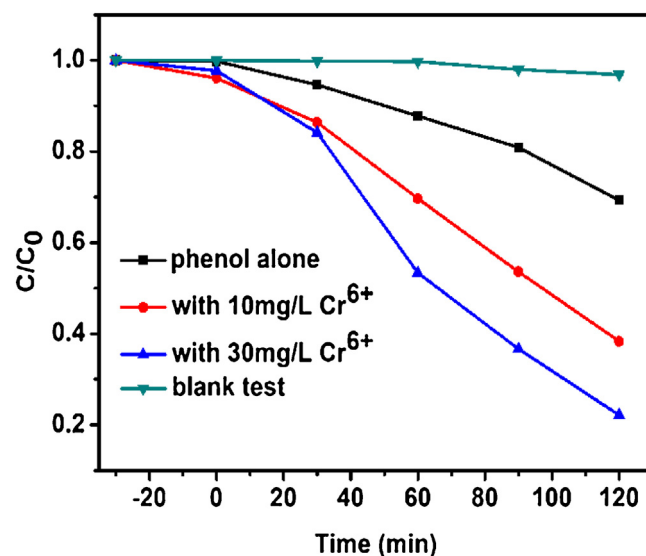


Fig. 12. Effect of Cr (VI) concentration on the photocatalytic degradation of phenol (10 mg/L) by using 50:1 Ti-SBA15-CN under visible light irradiation (blank test: degradation of 10 mg/L phenol with 10 mg/L Cr (VI) without catalyst).

30 mg/L phenol, the reduction ratio of Cr (VI) over 50:1 Ti-SBA15-CN reached 100% after 120 min visible light irradiation, but the reduction ratio of Cr (VI) without phenol was just less than 20%.

#### 3.2.3. Effect of Cr (VI) concentration on the photocatalytic degradation of phenol

Similarly, the presence of Cr (VI) significantly promoted the degradation rate of phenol. The effect of Cr (VI) concentration on the photocatalytic degradation of 10 mg/L phenol was studied by increasing the Cr (VI) concentration from 0 to 30 mg/L at  $\text{pH} = 2.3$ . As shown in Fig. 12, the degradation of phenol gradually increased with the increasing Cr (VI) concentration. For example, the removal rate of phenol in presence of 30 mg/L Cr (VI) was nearly three times higher than in its absence. These results further confirmed the synergistic effect between the reduction of Cr (VI) and the oxidation of phenol.



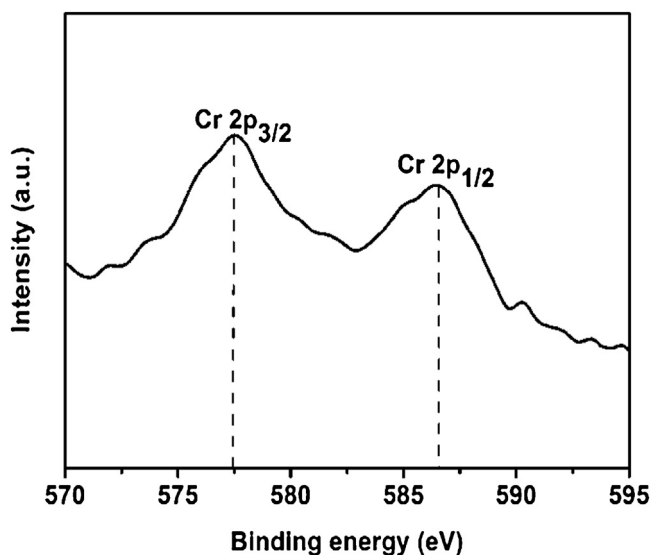


Fig. 13. Cr 2p spectrum of chromium on 50:1 Ti-SBA15-CN after photoreaction.

### 3.2.4. The byproducts of the photocatalytically treated Cr (VI) and phenol

To confirm the byproduct of Cr (VI) photoreduction, the XPS spectrum of the Cr adsorbed on the catalyst after photoreaction was analyzed, as shown in Fig. 13. From the figure, significant binding energies at 577.4 and 586.6 eV could be observed, which could be attributed to Cr(III), corresponding to the 2p<sub>3/2</sub> and 2p<sub>1/2</sub> orbitals respectively [42]. This result implied that Cr (VI) was reduced to Cr (III) during the photoreaction.

For the degradation of phenol, in our work, 1,4-benzoquinone was detected as the main byproduct by HPLC, as shown in Fig. 14a. Besides this ring byproduct, there may be some ring-opening byproducts like short chain acids [43]. However, the ring-opening byproducts could not be identified by HPLC and they were not identified by using other analytical methods in this work. Instead, the TOC was performed to determine the degree of mineralization. From Fig. 14b, it could be seen that the TOC removal values were gradually increased. This was understandable since degradation of phenol took time until being finally mineralized [44]. All things considered, we could speculate that the phenol was first oxidized to 1,4-benzoquinones and finally mineralized to CO<sub>2</sub> and H<sub>2</sub>O, which

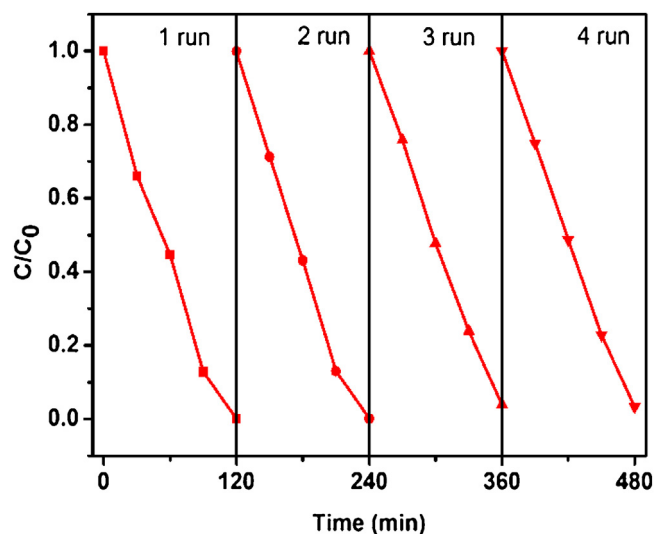


Fig. 15. Effect of cycling runs on 10 mg/L Cr (VI) reduction with 30 mg/L phenol in the presence of 50:1 Ti-SBA15-CN under visible-light irradiation.

was consistent with the previous reports about the scheme of phenol degradation [44].

### 3.2.5. Stability test

Besides the photocatalytic activity, the photocatalytic stability was another essential factor for a photocatalyst. The photocatalytic stability of 50:1 Ti-SBA15-CN was investigated by the recycling experiments. After every cycle, the suspension was filtered to regenerate the photocatalysts and reused in the next cycle. Fig. 15 showed that the photoreduction degree of Cr (VI) still remained high after 4 cycles, indicating the catalyst exhibited good visible-light photocatalytic stability.

### 3.2.6. Mechanism

To investigate the mechanism for the enhancement of the photocatalytic activity by the combination of carbon nitride and Ti species in SBA-15, photoluminescence (PL) spectra were measured, which has been proved to be an effective way to investigate the separation efficiency of photo-generated electrons and holes [45–47]. Fig. 16 showed the PL spectra of the as-prepared photocatalysts excited at 360 nm. The SBA15-CN exhibited a PL emission band at 460 nm. This peak could be attributed to the recombina-

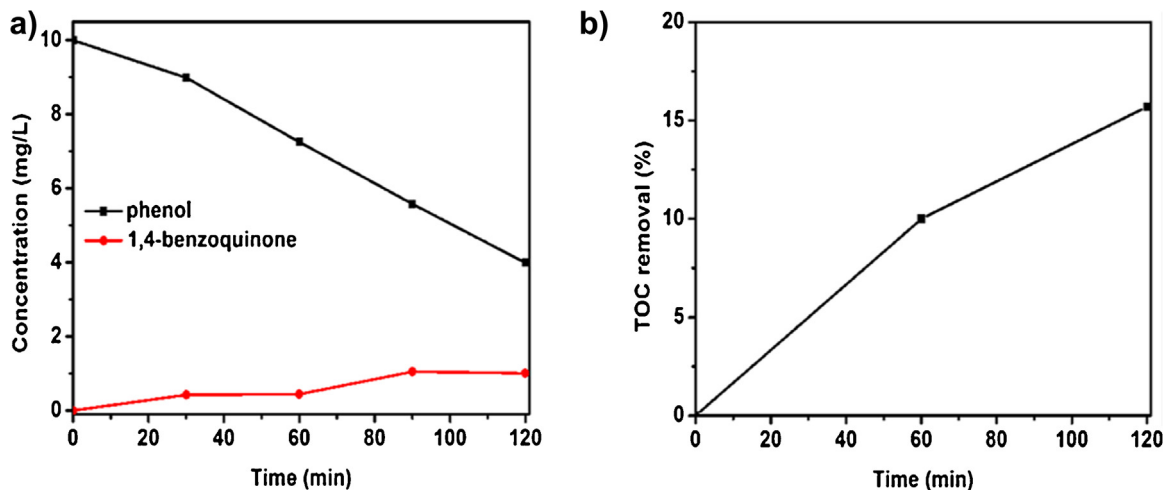


Fig. 14. (a) Concentrations for phenol and byproduct analyzed by HPLC. (b) TOC removal yield of 10 mg/L phenol solution with 10 mg/L Cr (VI).



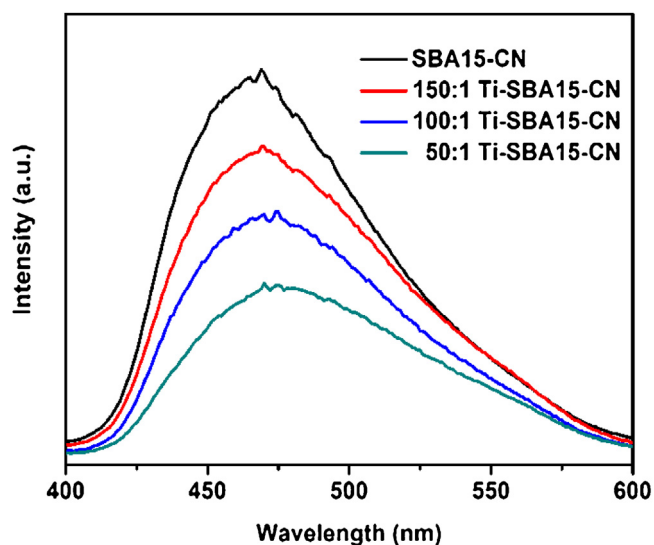


Fig. 16. PL emission spectra of SBA15-CN and Ti-SBA15-CN photocatalysts.

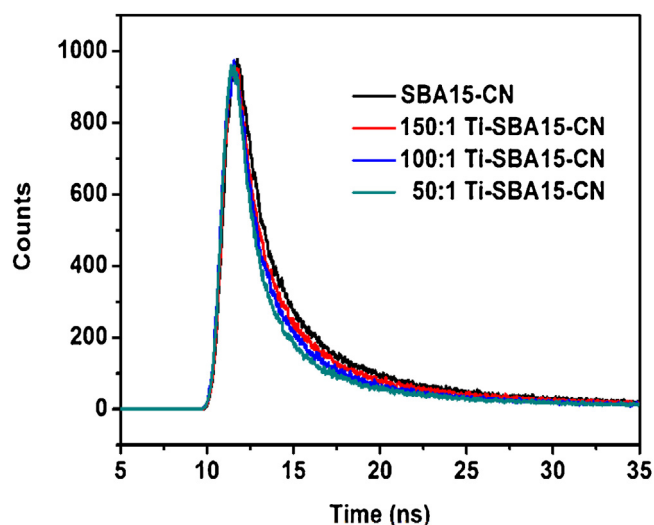


Fig. 17. PL emission decay curves for SBA15-CN and Ti-SBA15-CN. Observation wavelength for all the samples was 470 nm and excitation wavelength was 360 nm.

tion of the photo-generated electron-hole pairs in carbon nitride. When compared with SBA15-CN, the PL intensity was reduced by introducing Ti into the SBA-15 framework structure for the Ti-SBA15-CN, indicating the improvement in separation efficiency of the photo-generated electron-hole pairs. This was because the photo-generated electrons in carbon nitride could be easily transferred to the Ti moiety in Ti-SBA15 framework. In addition, with the increase of Ti contents in Ti-SBA15-CN, the PL intensity was gradually declined, meaning the photo-generated electron-hole recombination could be efficiently inhibited.

In addition to the PL emission spectra, PL emission decay spectra (Fig. 17) of SBA15-CN and Ti-SBA15-CN samples were also measured to further confirm the efficient charge separation between Ti-SBA15 and carbon nitride. The average lifetime of the carriers ( $\tau_{\text{avg}}$ ) of SBA15-CN, 150:1 Ti-SBA-CN, 100:1 Ti-SBA15-CN and 50:1 Ti-SBA15-CN were 6.56 ns, 6.15 ns, 5.33 ns and 5.22 ns respectively, as shown in Table 2, indicating that the charge transfer in carbon nitride was effectively enhanced when combined with Ti-SBA15. Since the photo-generated electrons in carbon nitride could be easily trapped by the Ti moiety in Ti-SBA15 framework, Ti-SBA15-CN showed shorter carrier lifetime than SBA15-CN. In addition, with

**Table 2**

Kinetic parameters of the emission decay analysis of different photocatalysts.

Samples	$\tau_1$ (ns)	$\tau_2$ (ns)	$\tau_{\text{avg}}$ (ns)	$\chi^2$
SBA15-CN	2.15 (52.6%)	11.45 (47.4%)	6.56	1.154
150:1 Ti-SBA15-CN	2.07 (53.5%)	10.85 (46.5%)	6.15	1.179
100:1 Ti-SBA15-CN	1.85 (57.08%)	9.96 (42.92%)	5.33	1.125
50:1 Ti-SBA15-CN	1.67 (58.86%)	10.30 (41.14%)	5.22	1.15

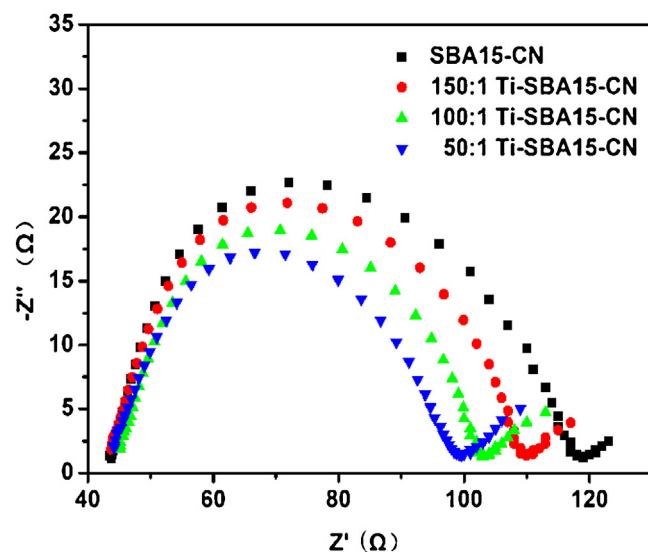
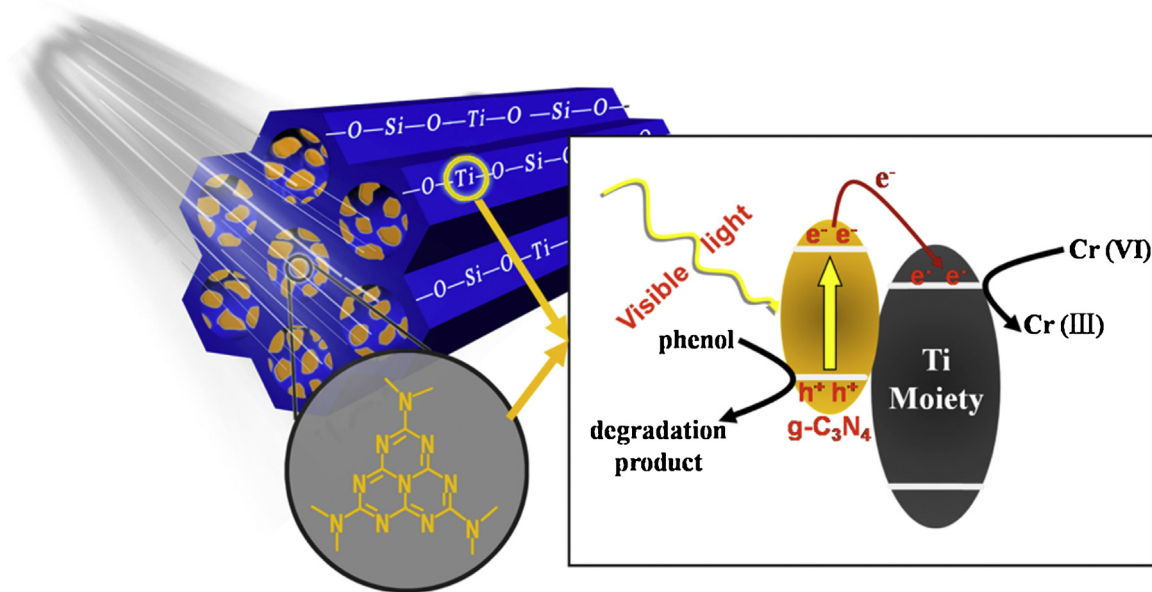


Fig. 18. Electrochemical Impedance Spectroscopy of Ti-SBA15-CN.

the increase of Ti contents in Ti-SBA15-CN, the carrier lifetime was gradually declined, meaning the charge separation between Ti-SBA15 and carbon nitride was further improved [48].

Besides the photoluminescence measurement and photoluminescence emission decay spectra, we also use electrochemical impedance spectroscopy (EIS) to investigate the charge transfer resistance of the catalysts [49–51]. The EIS results of Ti-SBA15-CN were presented in Fig. 18 in the form of Nyquist plots. From the figure we could see that SBA15-CN had a large arc radius, meaning a high charge transport resistance of the material. The charge transport resistance of the Ti-SBA15-CN was smaller than SBA15-CN, and with the increase of Ti contents, the resistance became more and more small. This result suggested that an effective separation of photo-generated electron-hole pairs and faster charge transfer occurred on the Ti-SBA15-CN.

From the above results, it could be seen that the existence of Ti moiety could contribute to the superior photocatalytic properties of Ti-SBA15-CN. It was well-known that Ti moieties mainly existed in the Ti-SBA15 framework. Then the charge transfer process and photocatalytic mechanism of Ti-SBA15-CN could be depicted in Scheme 1. Upon visible light irradiation, carbon nitride was photo-excited to produce CB electrons and VB holes, and the CB electrons in carbon nitride could easily transfer to the Ti moiety which could donate electrons to Cr (VI) reduction, while the holes left on the conduction band of carbon nitride cause the oxidation of phenol. This catalytic could effectively separate electrons and holes in carbon nitride, leading to higher photocatalytic activity of Ti-SBA15-CN than SBA15-CN. In addition, with the increase of Ti contents, much more electrons and holes in carbon nitride were separated, so the photocatalytic activity of Ti-SBA15-CN exhibited a rise with the increase of Ti contents.



**Scheme 1.** Proposed photocatalytic mechanism in Ti-SBA15-CN.

#### 4. Conclusion

In conclusion, carbon nitride had been successfully loaded into the Ti-SBA15. Enhanced visible light induced photocatalytic reduction of Cr (VI) was achieved over Ti-SBA15-CN and a scheme of Cr (VI) reduction over Ti-SBA15-CN was proposed. Upon irradiation by visible light, the photogenerated electrons in the conduction band of carbon nitride could be easily transferred to the Ti moiety in Ti-SBA15 framework, and then captured by Cr (VI) which was reduced to Cr (III). The addition of phenol promoted the photocatalytic reduction of Cr (VI) over Ti-SBA15-CN under visible light irradiation as the photo-generated holes oxidized the phenol, leading to the further improved separation of the photo-generated electrons and holes in carbon nitride. Moreover, the presence of Cr (VI) significantly promoted the degradation of phenol, that was, an obvious synergistic effect was observed. This effective simultaneous photocatalytic reduction and oxidation processes provided the dual benefits for the environment remediation and purification processes.

#### Acknowledgements

This work was financially supported by National Nature Science Foundation of China (21407049, 21377038, 21237003), National Key Research and Development Program (2016YFA0204200), China Postdoctoral Science Foundation (2015T80409), Shanghai Pujiang Program (14PJ1402100).

#### References

- [1] L.H. Keith, W.A. Telliard, *Environ. Sci. Technol.* 13 (1979) 416–423.
- [2] J.J. Testa, M.A. Grela, M.I. Litter, *Environ. Sci. Technol.* 38 (2004) 1589–1594.
- [3] F. Fu, Q. Wang, *J. Environ. Manag.* 92 (2011) 407–418.
- [4] L.M. Torres-Martínez, E. Moctezuma, M.A. Ruiz-Gómez, I. Juárez-Ramírez, M.Z. Figueroa-Torres, *Res. Chem. Intermed.* 39 (2013) 1533–1544.
- [5] X.F. Hu, H.H. Ji, F. Chang, Y.M. Luo, *Catal. Today* 224 (2014) 34–40.
- [6] D. Fabbri, A.B. Prevot, E. Pramauro, *Appl. Catal. B: Environ.* 62 (2006) 21–27.
- [7] M.R. Prairie, L.R. Evans, B.M. Stange, S.L. Martinez, *Environ. Sci. Technol.* 27 (1993) 1776–1782.
- [8] S. Sajjad, S.A.K. Leghari, F. Chen, J. Zhang, *Chem. Eur. J.* 16 (2010) 13795–13804.
- [9] D. Ji, J. Zhu, Min Ji, Yang Leng, *Res. Chem. Intermed.* (2015), <http://dx.doi.org/10.1007/s11164-015-2375-9>.
- [10] A.D. Mani, P.M.K. Reddy, M. Srinivas, P. Ghosal, N. Xanthopoulos, Ch. Subrahmanyam, *Mater. Res. Bull.* 61 (2015) 391–399.
- [11] Z. Jin, Y.X. Zhang, F.L. Menga, Y. Jia, T. Luo, X.Y. Yu, J. Wang, J.H. Liu, X.J. Huang, *J. Hazard. Mater.* 276 (2014) 400–407.
- [12] J. Lei, Y. Chen, F. Shen, L. Wang, Y. Liu, J. Zhang, *J. Alloy Compd.* 631 (2015) 328–334.
- [13] J. Lei, Y. Chen, L. Wang, Y. Liu, J. Zhang, *J. Mater. Sci.* 50 (2015) 3467–3476.
- [14] H. Li, L. Wang, Y. Liu, J. Lei, J. Zhang, *Res. Chem. Intermed.* 42 (2016) 3979–3998.
- [15] S.C. Yan, Z.S. Li, Z.G. Zou, *Langmuir* 25 (2009) 10397–10401.
- [16] F. Chang, Y.C. Xie, C.L. Li, J. Chen, J.R. Luo, X.F. Hu, J.W. Shen, *Appl. Surf. Sci.* 280 (2013) 967–974.
- [17] Q.J. Fan, Y.N. Huang, C. Zhang, J.J. Liu, L.Y. Piao, Y.C. Yu, S.L. Zuo, B.S. Li, *Catal. Today* 264 (2016) 250–256.
- [18] D.Y. Zhao, J.L. Feng, Q.S. Huo, N. Melosh, G.H. Fredrickson, B.F. Chmelka, G.D. Stucky, *Science* 279 (1998) 548–552.
- [19] D.Y. Zhao, Q.S. Huo, J.L. Feng, B.F. Chmelka, G.D. Stucky, *J. Am. Chem. Soc.* 120 (1998) 6024–6036.
- [20] H. Li, L. Zhou, L.Z. Wang, Y.D. Liu, J. Lei, J.L. Zhang, *Phys. Chem. Chem. Phys.* 17 (2015) 17406–17412.
- [21] S.W. Zhang, L.P. Zhao, M.Y. Zeng, J.X. Li, J.Z. Xu, X.K. Wang, *Catal. Today* 224 (2014) 114–121.
- [22] H. Li, X. Shen, Y. Liu, L. Wang, J. Lei, J. Zhang, *J. Alloy Compd.* 646 (2015) 380–386.
- [23] D.Y. Qi, L.J. Lu, Z.H. Xi, L.Z. Wang, J.L. Zhang, *Appl. Catal. B: Environ.* 160 (2014) 621–628.
- [24] P. Wang, J. Lei, M. Xing, L. Wang, Y. Liu, J. Zhang, *J. Environ. Chem. Eng.* 3 (2015) 961–968.
- [25] J. Lei, L. Yang, D. Lu, X. Yan, C. Cheng, Y. Liu, L. Wang, J. Zhang, *Adv. Opt. Mater.* 3 (2015) 57–63.
- [26] J. Lei, L. Wang, J. Zhang, *ACS Nano* 5 (2011) 3447–3455.
- [27] J. Lei, L. Wang, J. Zhang, *Chem. Commun.* 46 (2010) 8445–8447.
- [28] J.R. Martinez, F. Ruiz, Y.R. Vorobiev, J.F. Perez-Robles, J. Gonzalez-Hernandez, *J. Chem. Phys.* 109 (1998) 7511–7514.
- [29] L. Ge, F. Zuo, J. Liu, Q. Ma, C. Wang, D. Sun, L. Bartels, P. Feng, *J. Phys. Chem. C* 116 (2012) 13708–13714.
- [30] M. Shalom, S. Inal, D. Neher, M. Antonietti, *Catal. Today* 225 (2014) 185–190.
- [31] Y. Kong, H.Y. Zhu, G. Yang, X.F. Guo, W.H. Hou, Q.J. Yan, M. Gu, C. Hu, *Adv. Funct. Mater.* 14 (2004) 816–820.
- [32] C. Ronning, H. Feldermann, R. Merk, H. Hofsass, *Phys. Rev. B* 58 (1999) 2207–2214.
- [33] F. Le Normand, J. Hommet, T. Szorenyi, C. Fuchs, E. Fogarassy, *Phys. Rev. B* 64 (2001) 235416–235420.
- [34] K. Ikeue, H. Yamashita, M. Anpo, *J. Phys. Chem. B* 105 (2001) 8350–8355.
- [35] C. Cheng, D. Lu, B. Shen, Y. Liu, J. Lei, L. Wang, J. Zhang, M. Matsuoka, *Micro. Meso. Mater.* 226 (2016) 79–87.
- [36] L. Marchese, T. Maschmeyer, E. Gianotti, S. Coluccia, J.M. Thomas, *J. Phys. Chem. B* 101 (1997) 8836–8838.
- [37] L. Marchese, E. Gianotti, V. Dellarocca, T. Maschmeyer, F. Rey, S. Coluccia, J.M. Thomas, *Phys. Chem. Chem. Phys.* 1 (1999) 585–592.
- [38] M. Anpo, N. Aikawa, Y. Kubokawa, M. Che, C. Louis, E. Giamello, *J. Phys. Chem.* 89 (1985) 5017–5021.

- [39] T. Kamegawa, N. Suzuki, K. Tsuji, J.J. Sonoda, Y. Kuwahara, K. Mori, H. Yamashita, *Appl. Catal. B: Environ.* 175 (2011) 393–397.
- [40] R. Velmurugan, M. Swaminathan, *Res. Chem. Intermed.* 41 (2015) 1227–1241.
- [41] J. Chen, S.H. Shen, P.H. Guo, M. Wang, P. Wu, X.X. Wang, L.J. Guo, *Appl. Catal. B: Environ.* 152–153 (2014) 335–341.
- [42] H. Figueiredo, B. Silva, I. Kuz'niarska-Biernacka, A.M. Fonseca, R. Medina, S. Rasmussen, M.A. Banares, I.C. Neves, T. Tavares, *Chem. Eng. J.* 247 (2014) 134–141.
- [43] E. Grabowska, J. Reszczynska, A. Zaleska, *Water Res.* 46 (2012) 5453–5471.
- [44] A.M. Al-Hamdi, M. Sillanpää, J. Dutta, *J. Mater. Sci.* 49 (2014) 5151–5159.
- [45] B. Subash, B. Krishnakumar, M. Swaminathan, M. Shanthi, *Res. Chem. Intermed.* 39 (2013) 3181–3197.
- [46] K. Yadav, M. Giri, N. Jaggi, *Res. Chem. Intermed.* 41 (2015) 9967–9978.
- [47] A.K.L. Sajjad, S. Shamaila, B.Z. Tian, F. Chen, J.L. Zhang, *Appl. Catal. B: Environ.* 91 (2009) 397–405.
- [48] S. Sardar, P. Kar, H. Remita, B. Liu, P. Lemmens, S.K. Pal, S. Ghosh, *Sci. Rep.* 5 (2015) 17313–17326.
- [49] C. Zeng, M. Guo, B. Tian, J. Zhang, *Chem. Phys. Lett.* 575 (2013) 81–85.
- [50] C. Zeng, B. Tian, J. Zhang, *J. Colloid, Interface Sci.* 405 (2013) 17–21.
- [51] X. Liu, L.J. Chen, R.Y. Chen, Z. Chen, X. Chen, X. Zheng, *Res. Chem. Intermed.* 41 (6) (2015) 3623–3636.